

Strain dependence of Auger recombination in $3\ \mu\text{m}$ GaInAsSb/GaSb type-I active regions

Cite as: Appl. Phys. Lett. **116**, 262103 (2020); <https://doi.org/10.1063/5.0007512>

Submitted: 13 March 2020 . Accepted: 16 June 2020 . Published Online: 30 June 2020

Kenneth J. Underwood , Andrew F. Briggs , Scott D. Sifferman , Varun B. Verma, Nicholas S. Sirica, Rohit P. Prasankumar , Sae Woo Nam, Kevin L. Silverman, Seth R. Bank , and Juliet T. Gopinath 



View Online



Export Citation



CrossMark

Lock-in Amplifiers
up to 600 MHz



Strain dependence of Auger recombination in $3\ \mu\text{m}$ GaInAsSb/GaSb type-I active regions

Cite as: Appl. Phys. Lett. **116**, 262103 (2020); doi: [10.1063/5.0007512](https://doi.org/10.1063/5.0007512)

Submitted: 13 March 2020 · Accepted: 16 June 2020 ·

Published Online: 30 June 2020



View Online



Export Citation



CrossMark

Kenneth J. Underwood,^{1,a)} Andrew F. Briggs,² Scott D. Sifferman,² Varun B. Verma,³ Nicholas S. Sirica,⁴ Rohit P. Prasankumar,⁴ Sae Woo Nam,³ Kevin L. Silverman,³ Seth R. Bank,² and Juliet T. Gopinath^{1,5}

AFFILIATIONS

¹Department of Physics, University of Colorado Boulder, Boulder, Colorado 80309, USA

²Department of Electrical and Computer Engineering, University of Texas Austin, Austin, Texas 78758, USA

³National Institute of Standards and Technology, 325 Broadway, Boulder, Colorado 80305, USA

⁴Center for Integrated Nanotechnologies, Los Alamos National Laboratory, Los Alamos, New Mexico 87545, USA

⁵Department of Electrical, Computer, and Energy Engineering, University of Colorado Boulder, Boulder, Colorado 80309, USA

^{a)} Author to whom correspondence should be addressed: kenneth.underwood@colorado.edu

ABSTRACT

We differentiate the effect of strain induced by lattice-mismatched growth from strain induced by mechanical deformation on cubic nonradiative Auger recombination in narrow-gap GaInAsSb/GaSb quantum well (QW) heterostructures. The typical reduction in the Auger coefficient observed with lattice-mismatched growth appears to be due to the concomitant compositional change rather than the addition of strain, with implications for mid-IR semiconductor laser design. We induced a range of internal compressive strain in five samples from -0.90% to -2.07% by varying the composition during the growth and mechanically induced a similar range of internal strain in analogous quantum well membrane samples. We performed time-resolved photoluminescence and differential reflectivity measurements to extract the carrier recombination dynamics, taken at 300 K with carrier densities from $2.7 \times 10^{18}\ \text{cm}^{-3}$ to $1.4 \times 10^{19}\ \text{cm}^{-3}$. We observed no change with strain in the cubic Auger coefficient of samples that were strained mechanically, but we did observe a trend with strain in samples that were strained by the QW alloy composition. Measured Auger coefficients ranged from $3.0 \times 10^{-29}\ \text{cm}^6\ \text{s}^{-1}$ to $3.0 \times 10^{-28}\ \text{cm}^6\ \text{s}^{-1}$.

Published under license by AIP Publishing. <https://doi.org/10.1063/5.0007512>

The mid-infrared (mid-IR) spectral region from 2 to $5\ \mu\text{m}$ is of significant technological interest due to applications in trace gas sensing (CH_4 , CO_2 , SO_2 , etc.),^{1,2} disease recognition and treatment,³ free space communications,⁴ and defense.⁵ Semiconductor lasers, such as intersubband quantum cascade lasers (QCLs), type-II interband cascade lasers (ICLs), and type-I diode lasers, can generate mid-IR light at low cost with high wall-plug efficiency.⁶ Type-I diode lasers in the mid-IR, typically composed of compressively strained GaInAsSb quantum wells (QWs) with barriers of GaSb or lattice-matched AlGaAsSb or AlGaInAsSb, have achieved comparable performance to QCLs and ICLs below $3\ \mu\text{m}$.⁷ Performance beyond $3\ \mu\text{m}$ with such lasers has been plagued by issues with carrier capture, free-carrier absorption, and Auger recombination, with as much as 80% of excited carriers at threshold lost to Auger recombination.⁸ Reducing such nonradiative recombination is critical for achieving high efficiencies. Tailoring the alloy composition of the barriers in such devices allows researchers to increase hole capture and can improve device performance, but such adjustments tend to also increase free carrier

absorption.⁹ Using GaSb barriers avoids this issue, but the reduced hole confinement still results in poor lasing efficiency.¹⁰ Due to the type-I geometry, increasing the quantum well Sb percentage can increase hole confinement without requiring complex barrier compositions.⁶ This increased Sb percentage also increases the compressive strain, which should decrease Auger losses, as compressive strain breaks the heavy-hole–light-hole (HH–LH) degeneracy and lowers the effective HH mass. This lower mass decreases the hole quasi-Fermi level at threshold, reducing the carrier density required for gain and proportionately reducing losses from Auger.^{11,12} Improvements in laser performance have been observed in such highly strained mid-IR GaInAsSb/GaSb devices.¹³

The reduced effective HH mass not only will decrease the carrier density at threshold but could also decrease the Auger coefficient itself, with a strong impact on the CHHS Auger process [one conduction band (CB) state, two HH states, and one spin–orbit (SO) state], which dominates for near-IR semiconductors.¹⁴ Recent work strongly suggests that CCCH is the driving factor for parasitic Auger loss in

GaInAsSb/GaSb mid-IR devices,^{15,16} which could alter the impact of mechanical strain on the Auger coefficient for such narrow-gap GaSb-based devices. In this paper, we differentiate between the effect changes in strain due to the alloy composition and changes in strain due to external stress have on Auger recombination in narrow-gap, highly strained GaInAsSb/GaSb active regions. We accomplish this using time-resolved carrier decay measurements of epitaxially strain-varied samples and mechanically strain-varied samples. We observe a notable performance difference between the two strain-adjustment techniques.

The heterostructures under test [shown in Fig. 1(b)] consisted of a stack of four 10-nm GaInAsSb wells surrounded by 20-nm GaSb barriers, sandwiched between ~200-nm GaSb spacing layers, emitting with peak photoluminescence (PL) at about 3 μm . Each sample was coated with a Ti/Au reflective backing layer. In the first set of samples, chips with varying As concentrations in the QWs were grown, inducing internal compressive strain ranging from -0.90% to -2.07% . These chips were bonded to rigid Mo heat sinks before selectively etching away the GaSb substrate and the lattice-matched InAsSb etch release layer (see the [supplementary material](#)). In the second set of samples, we grew chips with the same layer structure with an As concentration in the QWs that induced about -2% internal compressive strain, then bonded the chips to a flexible film, and etched away the GaSb substrate. The final sample was a 250 nm thick QW region with reflective backing, which could flex and stretch with the membrane without disadherence or cracking. In testing, we biaxially stretched the flexible membrane, reducing the internal compressive strain in the QWs by mechanically applying external tensile strain.

We performed time-resolved photoluminescence (TRPL) and differential reflection pump probe (PP) measurements of the above samples in a range of applied strains. We conducted TRPL studies with direct detection in the mid-infrared and performed differential reflection PP measurements on the epitaxially strain-varied samples. In both sample sets, we performed measurements in a range of excited carrier densities and simultaneously monitored the PL emission spectrum vs time, pump fluence, and applied strain. For the stretched samples, the peak emission wavelength increases with applied strain as

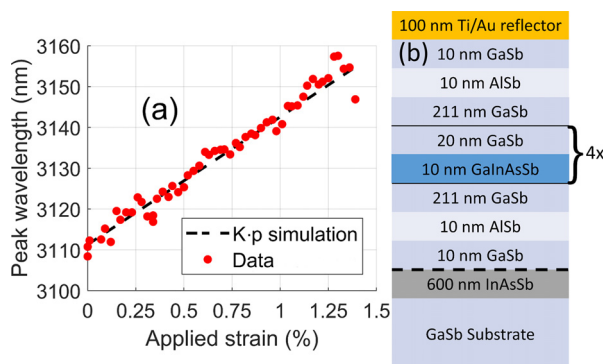


FIG. 1. (a) Peak photoluminescence wavelength with applied strain compared to the simulated shift in the bandgap expected for the given applied strain. The bandgap shift is calculated using eight-band $k \cdot p$ simulations.¹⁷ (b) Sample layer structure. The Ti/Au reflector layer is bonded to either a flexible membrane or inflexible heat sink. The region below the dashed line is etched away prior to the measurement.

shown in Fig. 1(a), providing a useful metric for calibrating the biaxial stretcher to the internal strain of the sample. Given the likelihood of anisotropic stretching, the peak PL wavelength was monitored for each stretching position and calibrated to the internal strain using eight-band $k \cdot p$ simulations. As the stretching process is destructive for the membrane samples, we mounted and etched pieces of the same wafer on several different membranes, each of slightly different sizes and etch quality. Taken as a set, the samples approximate the behavior of the QW material under mechanical stress.

TRPL measurements were taken using a mid-infrared PL spectroscopy system, with a commercial mode-locked Ti:sapphire source emitting ~ 1 W of <100 fs pulses at 800 nm with an 80 MHz repetition rate used for carrier excitation. The laser was focused onto the samples using a 15 mm focal length off-axis gold-coated parabolic mirror and pulse-picked down by $10\times$ to decrease the average power below the onset of melting/chip damage, which allows complete carrier relaxation between successive pulses, enabling us to measure a time window ~ 100 ns wide after the excitation pulse. A fast TeO₂ acousto-optic modulator (AOM) was used for pulse picking and provided ~ 50 dB of extraneous pulse suppression outside of the ~ 10 ns electronic pass window. PL from 1 to 4 μm was collected by the off-axis parabolic mirror and filtered to remove the reflected pump light. The PL was then fiber coupled with ZBLAN patch cable into a He sorption fridge kept at <1 K containing a WSi superconducting nanowire single-photon detector (SNSPD), with short time resolution (<200 ps). Further detector performance is described in Ref. 18. A characteristic TRPL measurement of an epitaxially strained sample is shown in Fig. 2(a). We fit these decay curves with a cubic recombination rate differential equation solved using the Runge–Kutta method, which we then convolved with the instrument response to obtain our decaying peak function.

In the PP measurements, ~ 200 fs pulses from a Yb fiber laser at 1.04 μm excited electron–hole pairs in samples and ~ 140 fs pulses from a synchronously pumped optical parametric oscillator probed the reflectivity at the peak of the PL, ~ 2.9 – 3.0 μm . Representative data from the pump-probe measurements are shown in Fig. 2(b), along with a fit with a degenerate cubic carrier recombination rate equation using the same coefficients as for the TRPL.

In order to interpret data such as shown in Fig. 2, we must convert these signals into excited carrier densities. The PL intensity is expressed as a function of carrier density $J_{PL} = \Gamma B(n_i + \Delta n)(p_i + \Delta p)$, with n_i and p_i being the intrinsic electron and hole densities, Δn and Δp the excess electron and hole densities, B the radiative coefficient, and Γ the geometric collection factor.¹⁹ From eight-band $k \cdot p$ calculations, it is found that intrinsic carrier populations should be well below excess carrier levels (assuming minimal doping in wells and barriers), and so $n_i + \Delta n \approx \Delta n$; we assume $\Delta n = \Delta p$, which is reasonable for primarily band–band generation and recombination.²⁰ Therefore, the PL equation becomes $J_{PL} = \Gamma B n^2$. Normalizing the PL intensity to the $t = 0$ value eliminates the collection factor and radiative term, reducing the PL intensity to solely a function of the carrier density, $J_{PL, norm} = n^2/n_0^2$, with peak excited carrier density $n_0 = \frac{FR}{2E_{phot}t}(1 - e^{-\alpha T})$, with F the pulse fluence, α the absorption, R the reflectivity, E_{phot} the pump photon energy, T the GaSb spacer thickness, and t the combined well width.²¹

In the case of the PP measurements, conversion from PP signal $\Delta R/R$ to carrier density requires knowledge of the instantaneous carrier density for a given $\Delta R/R$, which is only available at time $t = 0$.

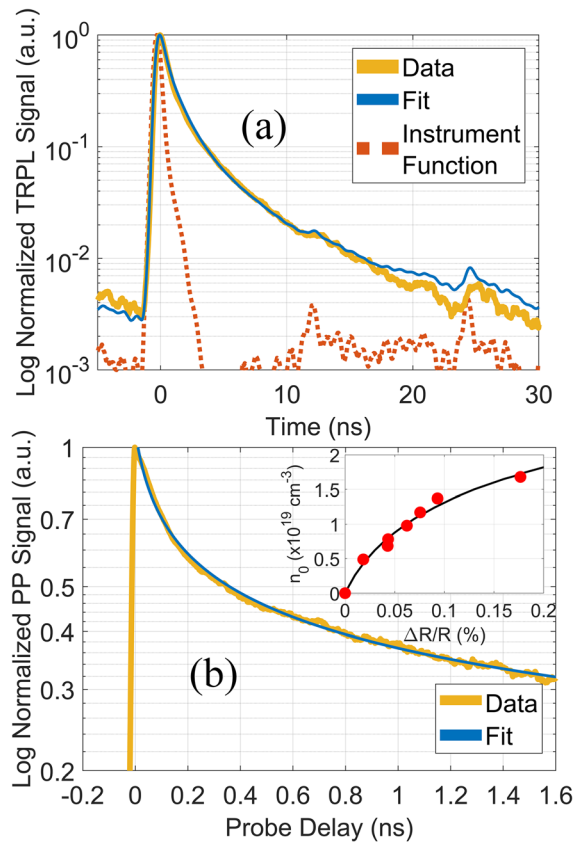


FIG. 2. Representative time-resolved measurements of an epitaxially strain-varied sample, by time-resolved (a) photoluminescence and (b) differential reflectivity pump-probe (PP). The inset in (b) shows the phenomenological fit between the PP peak value and known instantaneous peak carrier density n_0 . This functional dependence is used for converting the PP signal to an excited carrier density, necessary for fitting Auger recombination equations. Satellite peaks in (a) are due to imperfect AOM pulse-picking.

We use the same equation as above to find n_0 and then fit a phenomenological performance function f to the carrier density-reflectivity curve, as shown in the inset of Fig. 2(b). We can use the $n = f(\Delta R/R)$ relationship to transform $\Delta R/R$ into a time-dependent normalized carrier density,¹⁹ directly comparable to the TRPL result.

With both measurements in terms of excited carrier density, we can fit both the TRPL and PP results to a recombination rate,

$$\frac{d}{dt} \left(\frac{n}{n_0} \right) = A \frac{n}{n_0} + B n_0 \frac{n^2}{n_0^2} + C n_0^2 \frac{n^3}{n_0^3}, \quad (1)$$

with A the Shockley-Read-Hall (SRH) coefficient, B the radiative coefficient, and C the effective Auger coefficient.

Precise measurements of the cubic contributions to recombination decay can be achieved if the Auger lifetime approaches the SRH lifetime ($Cn^2 \sim A$). However, given the short SRH lifetime and low Auger coefficient of these heterostructures (as well as the narrow bandgap), we needed to excite our samples with high carrier densities, $>10\times$ beyond the degenerate carrier density limit, above carrier concentrations typical of diode laser thresholds.²² For nondegenerate

excitation densities, Auger processes are well described by Boltzmann statistics, but exciting as high as we have necessitates treating the Auger processes using Fermi statistics.^{22,23} Measurements with excited carrier densities higher than calculated diode laser thresholds were combined with measurements at lower excited carrier densities, obtaining a continuous convergence curve as the carrier concentrations excited the degenerate regime. Note that ABC coefficients from TRPL data were extracted in a time window where carrier density was significantly reduced from the degenerate peak (beginning ~ 1.5 ns after zero delay) in part due to the finite impulse response time of the SNSPD. This reduced the excited carrier density for ABC fitting by approximately 11 dB, into the regime of typical narrow-gap GaSb-based laser operation ($n \sim 10^{12}$ cm⁻² in the well²⁴).

In the nondegenerate case, the Auger coefficient is presumed to be independent of carrier density. However, in the degenerate case, the Auger coefficient is itself nonlinear with carrier density and contributes to the linear, quadratic, and cubic recombination rates. Thus, the Auger recombination rate is given by $C(n)n^X$.²⁵ The X term can range from 1 to 3, and so the Auger term can be approximated by $C(n) = C_1 n + C_2 n^2 + C_3 n^3$. Thus, the net recombination rate becomes

$$\frac{d}{dt} \left(\frac{n}{n_0} \right) = (A + C_1) \frac{n}{n_0} + (B + C_2) n_0 \frac{n^2}{n_0^2} + C_3 n_0^2 \frac{n^3}{n_0^3}. \quad (2)$$

In this case, the linear and quadratic Auger rates cannot be unambiguously distinguished from the SRH and radiative terms, respectively, but the cubic Auger C_3 term is separable. It should be noted that while the cubic contribution to the recombination rate is unambiguously discriminable from SRH and radiative contributions, there could still be cubic contributions to the decay from other effects, notably carrier leakage, which can play a significant role in devices designed to operate above $3 \mu\text{m}$ and could contribute cubically to the decay.^{26,27} Such effects are not discriminated here although efforts to distinguish between effective cubic Auger recombination (including carrier leakage) and pure Auger recombination through temperature-dependent measurements are still ongoing.

While the linear and quadratic decay coefficients are independent of carrier density, the cubic Auger term is not. C_3 values for different carrier densities fit well with a convergence equation,²⁸

$$C_3(n_0) = \frac{C_3^0}{1 + (n_0/n_C)}, \quad (3)$$

allowing us to extract a low carrier density cubic Auger rate C_3^0 for each sample, along with SRH and radiative contributions. A fit of the degenerate cubic Auger coefficients vs n_0 to convergence equation (3) for a representative sample measured with TRPL is shown in Fig. 3. For each epitaxially strain-varied sample, we fit with this rate equation for both pump-probe and TRPL data to confirm performance.

The values of the nondegenerate-carrier-density cubic Auger C_3^0 , effective radiative, and effective SRH coefficients are shown in Fig. 4. We observe that there is an obvious minimum in the Auger coefficient for samples grown with epitaxially varying strain [Fig. 4(a)]. However, there does not appear to be any significant trend in the Auger coefficient measured for samples with mechanically varying strain [Fig. 4(d)], and response vs external stress is quite flat across a range of internal strains/peak emission wavelengths. When a QW sample is grown with -1.69% internal strain, the Auger coefficient is $\sim 0.42 \times \pm 0.06$

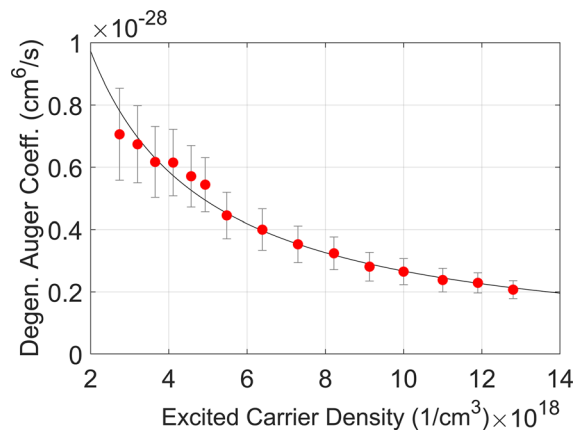


FIG. 3. Cubic Auger coefficients of a representative sample measured in a range of nominal excited carrier densities, all above the degenerate limit. The coefficients are fit to Eq. (3), from which we extract a low-carrier-density cubic Auger coefficient C_3^0 for each sample.

that of a sample grown with -0.9% strain and $\sim 0.27 \times \pm 0.05$ that of one grown with -2.07% strain. When a membrane sample is stretched to -1.69% , the average Auger coefficient is $1.12 \times \pm 0.14$ that of a sample stretched to -0.9% strain and $1.06 \times \pm 0.15$ that of the one stretched to -2.02% strain, with effectively no change. Note that there are minor structural differences between the epitaxially strain-varied samples and mechanically strain-varied samples, where the membrane samples only had one GaSb spacer region, on the gold mirror side of the QWs. This slight difference in the barrier regions will introduce error when comparing one sample set with another, which however, should not impact the trend observed in each set. Discussions of these structural differences are included in the [supplementary material](#).

The radiative coefficient measured for both sets of samples and in both experimental systems is consistently low, $\sim 10^{-11} - 10^{-12} \text{ cm}^3/\text{s}$ [Figs. 4(b) and 4(e)], in agreement with values reported for other sources for similar strained QW systems.²⁹ The SRH coefficient $< 10^8 \text{ 1/s}$ for both sample sets suggests good growth quality, and the consistency vs applied strain in the membrane suggests that the material system is not damaged on the scale of the diffusion length throughout the stretching process.

A notable effect of using binary GaSb barriers rather than AlGaAsSb or AlGaInAsSb barriers is a reduced valence band offset, even at pronounced compressive strain. This could increase the contribution of hole leakage to the cubic recombination term, particularly for small compressive strain at large As percentage in the well ($> 20\%$). Calculations based on the work of Chuang³⁰ (see the [supplementary material](#)) suggest that the reduced hole confinement commensurate with increased As percentage is also present for increased external strain and, thus, should contribute to the cubic coefficients extracted from the membrane samples as well. Further work calculating the impact of the valence band offset and carrier effective masses on cubic recombination in such devices is ongoing.

These measurements indicate that the reduction in the Auger coefficient of a narrow-gap strained heterostructure is predominately due to the alloy compositional change in the well, rather than due to mechanical stress. The results advance the notion that primarily

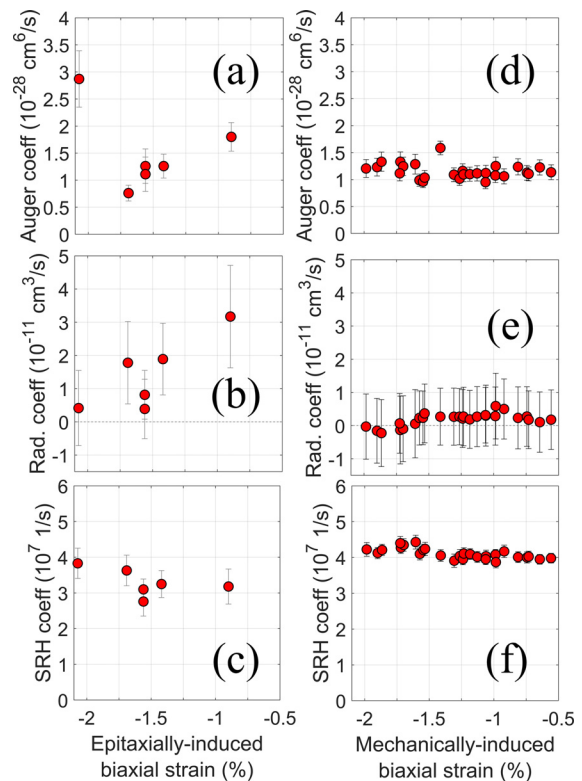


FIG. 4. Recombination coefficients for the epitaxially strained samples, (a) Auger, (b) radiative, and (c) SRH and for a mechanically strained membrane sample, (d) Auger, (e) radiative, and (f) SRH. The membrane results are plotted against the predicted internal strain found using the peak PL emission wavelength as in Fig. 1(a), where increasing mechanical strain would decrease the magnitude of the internal strain, and so the right-hand side of the plots corresponds to the highest degree of stretching. Epitaxially strained samples are plotted against calculated strain for their alloy percentages, with atomic spacing confirmed by high-resolution X-ray diffraction (HRXRD). The internal strain of the mechanically strained samples is the sum of the built-in strain from epitaxial growth and the strain from mechanical deformation (calculated as $\Delta L/L$), where increasing mechanical strain decreases the magnitude of the internal strain.

mechanical descriptions of Auger strain tuning are insufficient, particularly for narrow band GaSb-based devices and large amounts of internal strain. Reduced hole confinement may also play a significant role in these measurements, but does not appear to have a direct relationship given the difference in the performance of externally and internally applied strain. Changing the relative spacing of the SO, LH, HH, and conduction bands by alloy concentration plays a more significant role in reducing the Auger coefficient than reducing the HH mass for such systems, which has potent implications for future mid-IR device designs.

See the [supplementary material](#) for details on sample growth, membranes, the membrane-stretcher, and the PP system.

We acknowledge helpful technical support from Lange Simmons and Dr. Think Bui, as well as the support of the National Science Foundation (Grant Nos. DMR 1508783 and 1508603); the

Center for Integrated Nanotechnologies (CINT) (No. 2018BC0091); the Defense Advanced Research Projects Agency (DARPA) (No. W911NF-15-1-0621); and the Air Force Office of Scientific Research (AFOSR) (No. FA9550-15-1-0506).

DATA AVAILABILITY

The data that support the findings of this study are available within this article.

REFERENCES

- ¹D. Popa and F. Udrea, *Sensors* **19**, 2076 (2019).
- ²P. Werle and A. Popov, *Appl. Opt.* **38**, 1494–1501 (1999).
- ³R. Waynant, I. Ilev, and I. Gannot, *Philos. Trans. R. Soc. B* **359**, 635 (2001).
- ⁴Y. Su, W. Wang, X. Hu, H. Hu, X. Huang, Y. Wang, J. Si, X. Xie, B. Han, H. Feng, Q. Hao, G. Zhu, T. Duan, and W. Zhao, *Opt. Express* **26**, 34515–34528 (2018).
- ⁵E. Lippert, M. Haakestad, and H. Fonnum, ‘High-energy mid-IR laser for defense against heat-seeking missiles,’ *SPIE Newsroom* (published online, 2014).
- ⁶S. D. Sifferman, H. P. Nair, R. Salas, N. T. Sheehan, S. J. Maddox, A. M. Crook, and S. R. Bank, *IEEE J. Sel. Top. Quantum Electron.* **21**, 1–10 (2015).
- ⁷L. Shterengas, R. Liang, G. Kipshidze, T. Hosoda, G. Belenky, S. S. Bowman, and R. L. Tober, *Appl. Phys. Lett.* **105**, 161112 (2014).
- ⁸K. O’Brien, S. Sweeney, A. Adams, S. Jin, C. Ahmad, B. Murdin, A. Salhi, Y. Rouillard, and A. Joullié, *Phys. Status Solidi B* **244**, 203–207 (2007).
- ⁹M. Grau, C. Lin, O. Dier, C. Lauer, and M.-C. Amann, *Appl. Phys. Lett.* **87**, 241104 (2005).
- ¹⁰T. Lehnhardt, M. Hümmer, K. Rießner, M. Müller, S. Höfling, and A. Forchel, *Appl. Phys. Lett.* **92**, 183508 (2008).
- ¹¹A. R. Adams, *Electron. Lett.* **22**, 249–250 (1986).
- ¹²E. Yablonovitch and E. Kane, *J. Light. Technol.* **4**, 504–506 (1986).
- ¹³G. Belenky, D. Donetski, L. Shterengas, T. Hosoda, J. Chen, G. Kipshidze, M. Kisin, and D. Westerfeld, *Proc. SPIE* **6900**, 1–4 (2008).
- ¹⁴M. Takeshima, *J. Appl. Phys.* **43**, 4114–4119 (1972).
- ¹⁵T. Eales, I. P. Marko, B. A. Ikyo, A. R. Adams, I. Vurgaftman, S. Arafim, S. Sprengel, M.-C. Amann, J. R. Meyer, and S. J. Sweeney, in *2017 Conference on Lasers and Electro-Optics Europe European Quantum Electronics Conference (CLEO/Europe-EQEC)*, CB26 (2017).
- ¹⁶A. Sugimura, *IEEE J. Quantum Electron.* **19**, 930–932 (1983).
- ¹⁷S. Birner, T. Zibold, T. Andlauer, T. Kubis, M. Sabathil, A. Trellakis, and P. Vogl, *IEEE T. Electron. Dev.* **54**, 2137–2142 (2007).
- ¹⁸L. Chen, D. Schwarzer, J. A. Lau, V. B. Verma, M. J. Stevens, F. Marsili, R. P. Mirin, S. W. Nam, and A. M. Wodtke, *Opt. Express* **26**, 14859–14868 (2018).
- ¹⁹B. V. Olson, E. A. Shaner, J. K. Kim, J. F. Klem, S. D. Hawkins, L. M. Murray, J. P. Prineas, M. E. Flatté, and T. F. Boggess, *Appl. Phys. Lett.* **101**, 092109 (2012).
- ²⁰B. C. Connelly, G. D. Metcalfe, H. Shen, and M. Wraback, *Appl. Phys. Lett.* **97**, 251117 (2010).
- ²¹R. Debusmann, U. Brauch, V. Hoffmann, M. Weyers, and M. Kneissl, *J. Appl. Phys.* **112**, 033110 (2012).
- ²²V. Chazapis, H. A. Blom, K. L. Vodopyanov, A. G. Norman, and C. C. Phillips, *Phys. Rev. B* **52**, 2516–2521 (1995).
- ²³A. Haug, *Solid-State Electron.* **21**, 1281–1284 (1978).
- ²⁴G. Belenky, L. Shterengas, G. Kipshidze, and T. Hosoda, *IEEE J. Sel. Top. Quant. Electron.* **17**, 1426–1434 (2011).
- ²⁵J. O. Drumm, B. Vogelgesang, G. Hoffmann, C. Schwender, N. Herhammer, and H. Fouckhardt, *Semicond. Sci. Technol.* **17**, 1115–1122 (2002).
- ²⁶S. Bank, L. Goddard, M. Wistey, H. Yuen, and J. Harris, *IEEE J. Sel. Top. Quantum Electron.* **11**, 1089–1098 (2005).
- ²⁷R. Olshansky, C. Su, J. Manning, and W. Powazinik, *IEEE J. Quantum Electron.* **20**, 838–854 (1984).
- ²⁸M. E. Flatté, C. H. Grein, T. C. Hasenberg, S. A. Anson, D.-J. Jang, J. T. Olesberg, and T. F. Boggess, *Phys. Rev. B* **59**, 5745–5750 (1999).
- ²⁹B. V. Olson, E. Kadlec, J. K. Kim, J. F. Klem, S. D. Hawkins, E. A. Shaner, and M. Flatté, *Phys. Rev. Appl.* **3**, 044010 (2015).
- ³⁰S. L. Chuang, *Physics of Photonic Devices* (John Wiley & Sons, 2009).